IEEE Access
Multidisciplinary | Rapid Review | Open Access Journal

Received May 11, 2020, accepted June 3, 2020, date of publication June 16, 2020, date of current version June 24, 2020.

Digital Object Identifier 10.1109/ACCESS.2020.3002818

Waveguide Quadruplet Diplexer for Multi-Beam Satellite Applications

JAVIER OSSORIO GARCÍA, JUAN CARLOS MELGAREJO LERMAS, SANTIAGO COGOLLOS, (Member, IEEE), VICENTE E. BORIA, (Fellow, IEEE), AND MARCO GUGLIELMI, (Life Fellow, IEEE)

Departamento de Comunicaciones, iTEAM, Universitat Politècnica de València, 46022 Valencia, Spain

Corresponding author: Javier Ossorio García (jaosgar@teleco.upv.es)

This work was supported in part by the MINECO (Spanish Government) through Research and Development Project under Grant TEC2016-75934-C4-1-R, and in part by the Research and Development Technicians under Grant PTA2015-10839-I.

ABSTRACT The objective of this paper is to describe the design of an innovative and low-cost diplexer for Ka-band multi-beam satellite applications. The device is based on the use of two quadruplets to implement a number of transmission zeros (TZs) thus obtaining high-selectivity quasi-elliptic transfer functions. The resulting diplexer structure is particularly flexible in terms of layout, does not require tuning and has an excellent high-power behavior. In addition to theory, we compare the results of our simulations with the measurements obtained with a manufactured breadboard. The comparison shows excellent agreement thereby fully validating both the design procedure, and the new diplexer structure.

INDEX TERMS Design, diplexer, elliptic response, microwave filter, multipactor, quadruplet, rectangular waveguide, satellite communications.

I. INTRODUCTION

Modern satellite communication systems are evolving from the classical bent-pipe configuration toward multi-beam payloads and antennas. This evolution is required to increase the bandwidth of the system and the total radiated power (see [1] and [2]). As a consequence, new more selective and compact passive components need to be developed to fit the new requirements [3], [4].

The diplexer is one of the key elements of multi-beam satellite payloads [5]. Diplexers are used to split or combine two different frequency channels that use the same antenna. The need for high power handling and low losses makes rectangular waveguide diplexers a very attractive solution for this application. In most cases, diplexer structures consist of a 3-port waveguide junction connecting two band-pass filters to a common port [6]. Many different solutions have been discussed in the technical literature [7]–[11]. Typically, each filter is connected to the common port with a length of waveguide that is adjusted to optimize the performance of the diplexer. Many different solutions have also been discussed with the objective of reducing the footprint of the diplexer (see for instance [12]–[14]). More recently, alternative designs have also been presented, in [15] and [16], implementing TZs in the filter performances to increase the selectivity and reduce the diplexer footprint.

In this context, therefore, the objective of this paper is to significantly extend the initial results presented in [17] by discussing the detailed design of a very compact, low-loss rectangular waveguide diplexer.

The additional material with respect to [17], is as follows:

1) An in-depth investigation providing a physical justification for the presence of additional TZs implemented with capacitive inter-resonator couplings.
2) The complete design procedure of the diplexer structure.
3) The theoretical verification of the full diplexer design through a comparison with commercial EM simulators.
4) The prediction of the high-power multipactor discharge behavior.
5) The validation of the new structure diplexer through a comparison with the measurement of a prototype fabricated using aluminum.

II. DIPLEXER SPECIFICATIONS

The specifications that we have chosen as a target for our diplexer design are as follows:

The associate editor coordinating the review of this manuscript and approving it for publication was Feng Lin.

This work is licensed under a Creative Commons Attribution 4.0 License. For more information, see https://creativecommons.org/licenses/by/4.0/

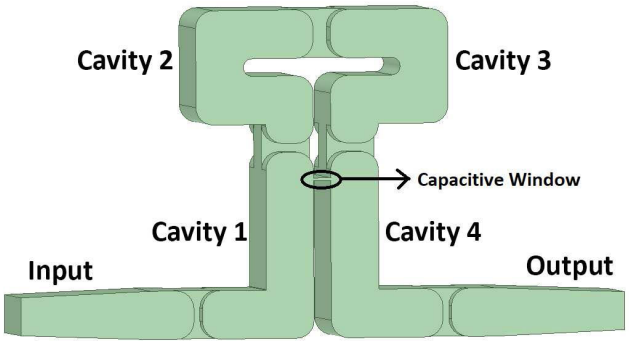

FIGURE 1. Quadruplet filter structure.

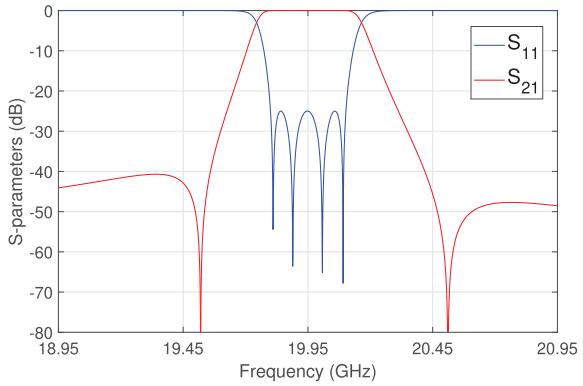

FIGURE 2. In-band response of the quadruplet filter.

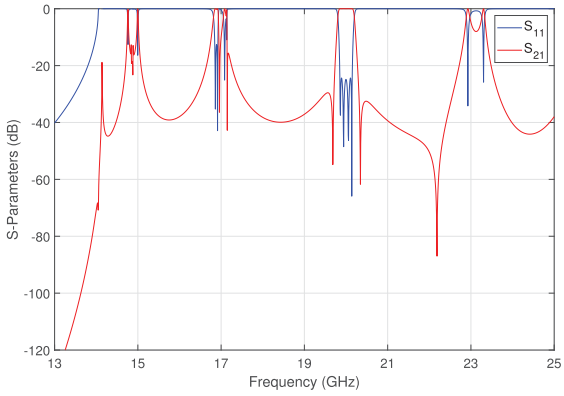

FIGURE 3. Out-of-band response of the quadruplet filter.

- I/O interface: WR-42
- Center frequency 1 (CF_1): 19.820 GHz
- Center frequency 2 (CF_2): 20.082 GHz
- Useful channel bandwidth (BW): 245 MHz
- In-band return loss (RL): $\geq$ 20 dB
- Insertion loss at CF_x: $\leq$ 0.3 dB
- Narrow band isolation:
  - Contiguous edge:
    $\geq$ 20 dB @ CF $\pm$ 144 MHz
    $\geq$ 40 dB @ CF $\pm$ 381 MHz
  - Non-contiguous edge:
    $\geq$ 20 dB @ CF $\pm$ 192 MHz
- Maximum operating RF input power: $\leq$ 200 W
- Maximum dimensions: $\leq$ 130 $\times$ 130 mm
- Maximum mass: $\leq$ 500 g

These specifications are inspired by the requirements for actual space applications for multi-beam payloads [18]. It is important to note, however, that the above specifications are not exactly identical to the ones indicated in [18]. This is because we realized, after significant efforts, that it was not possible to satisfy all the original requirements at the same time with a reasonable diplexer structure.

Our effort has, therefore, been devoted to the development of a *compact* structure that could give the best possible response with the smallest volume and a low fabrication cost. This situation is very common in the initial development activities for new payload configurations, where the main objective is to establish a proof of concept and not to deliver flight hardware.

Furthermore, following the design steps for the single quadruplet filter in [17], we have increased the return loss to 25 dB in the design process of the diplexer in order to have a margin to account for possible dimensional errors due to the fabrication process.

III. OUT OF BAND RESPONSE

Before going any further with the description of the design procedure for the diplexer, it is now appropriate to discuss the out-of-band behavior of the quadruplet filter shown in Fig. 1.

In Fig. 2 we recall the in-band response of the filter from [17].

Fig. 3 shows the out-of-band response of the same filter. As we can see, in the frequency range that we have simulated, there are four replicas of the filter pass band. The one we are interested in is the third. This is because the filter is designed to operate with the TE_{103} resonance. This choice, will produce larger cavities structures, however, as pointed out in [17], it will increase significantly the quality factor, and will eliminate the need for post-manufacturing adjustments (tuning screws).

As we mentioned already, the response of interest is the one centered at 20 GHz. However, if we look carefully at the S_{21} curve in Fig. 3, we can see that, in addition to the transmission zeros (TZs) near the pass-band, there are also two additional TZs.

The first additional TZ is located at about 17 GHz, that is inside the second pass band, whereas the second one is located at approximately 22 GHz.

In order to better understand the origin of the two additional TZs, we now focus our attention on the E-plane T-junction shown in Fig. 4. The performance of the T-junction was computed with CST Microwave Studio from CST (Computer Simulation Technology, now with Dassault Systèmes).

As we can see, this structure produces an alternating sequence of TZs and points of adaptation. Fig. 5 show the

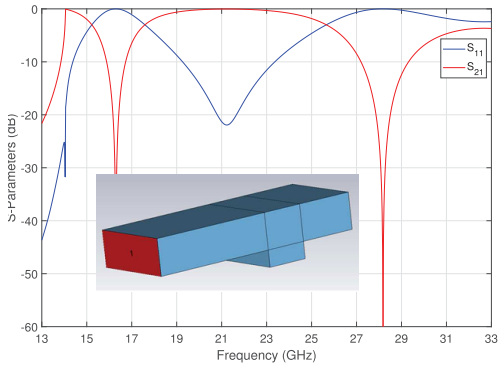

FIGURE 4. T-junction E-plane structure and performance in CST.

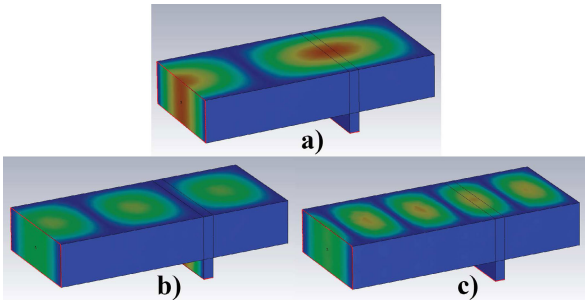

FIGURE 5. Electric fields distribution at the first TZ (a), frequency adaptation point (b) and second TZ (c).

electric field inside the T-junction at the frequencies of the first TZ, at the frequency of adaptation (S_{11} less than -20 dB), and at the frequency of the second TZ, respectively.

As we can clearly see, the electric field has a maximum just at the location of the T-junction when a TZ is produced. This is because the electric field has an even distribution with respect to the branch of the T-junction, so that the fundamental mode in the branch waveguide is not excited, hence the TZ.

At the frequency of adaptation, on the other hand, we can clearly see in Fig. 5 that the electric field has a strong odd component at the same location, thereby generating a point of adaptation for the fundamental mode of the branch waveguide.

This behavior is due to the interference between the E-plane T-Junction and the short-circuited end of the manifold. This is indeed well-known, and has been exploited in the past to define the optimum manifold configuration in manifold multiplexers [5] and, more recently, to generate transmission zeros in rectangular waveguide filters [19]. Our investigations indicate that this interference phenomenon is indeed the cause of the additional TZs that can be observed in the wide-band response in Fig. 3.

To further investigate this point, we now look at a simplified version of the quadruplet filter, namely, a two-pole filter with a capacitive inter-resonator coupling.

Fig. 6 shows the basic structure of the two-pole filter and the simulated wide-band performance. As we can

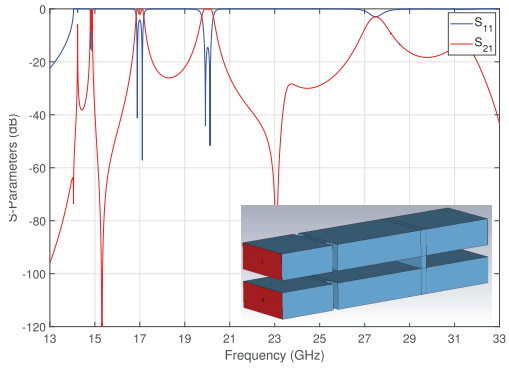

FIGURE 6. Structure and wide-band response of the two-pole filter with capacitive inter-resonator coupling.

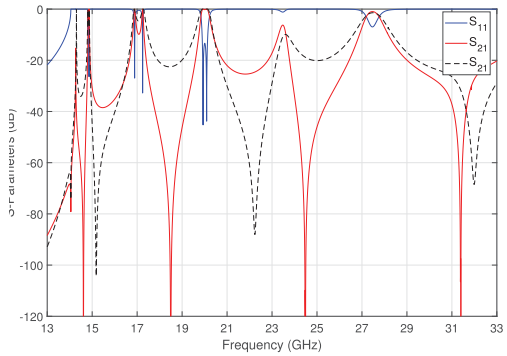

FIGURE 7. Two-pole filter with an additional TZ in the lower rejection band (continuous line) and an additional TZ in the higher rejection band (dashed line).

clearly see, this two-pole filer produces two TZs in the same approximate location as the one produced by the original quadruplet filter.

If we now change the distance of the capacitive iris from the end of the cavity to 18.0 mm, and to 12.0 mm, we obtain the results shown in Fig. 7.

As we can clearly see, changing the distance of the capacitive inter-resonator iris, we can effectively change the location of the additional TZs generated by the T-junction, while maintaining (via optimization) the same basic filter in-band response.

One last detail that is important to note is that since we actually need two T-junctions to implement a capacitive inter-resonator coupling, each one of the TZs is actually a *double* TZ.

This is clearly shown in Fig. 8, where we have introduced a slight asymmetry in the structure of the two-pole filter with the TZ in the lower rejection band (the continuous line in Fig.7).

This feature of the filter structure described in this paper can be very effectively exploited to design a diplexer, as will be shown in the reminder of this paper.

IV. DISTRIBUTED MODEL

To start the design of the diplexer, we first need to design two separate filters centered at the frequencies given in the

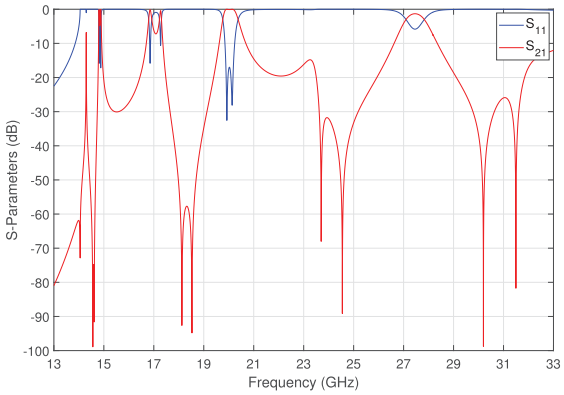

FIGURE 8. Two-pole filter with a double TZ in the lower rejection band.

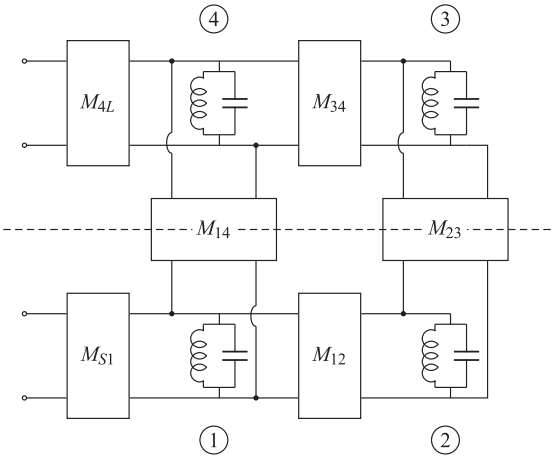

FIGURE 9. Lumped element circuit of a quadruplet.

specifications. Both filters are based on the basic rectangular waveguide quadruplet filter proposed in [17].

In this section, we are going to analyze and explain the behaviour of the quadruplet filter in terms of an equivalent distributed model.

A typical quadruplet topology with lumped elements for a 4-2 filter is the simple, well-known folded configuration shown in Fig. 9. Since the circuit is symmetric, we can write $M_{S1} = M_{4L}$ and $M_{12} = M_{34}$. For an in-band $RL > 20$ dB and rejection higher than 40 dB, we obtain the following values:

$$\begin{aligned} M_{S1} &= M_{4L} = 1.074145 \\ M_{12} &= M_{34} = 0.935874 \\ M_{23} &= 0.766639 \\ M_{14} &= -0.106916 \end{aligned} \tag{1}$$

To convert the lumped element circuit into a distributed one, we can replace the resonators with transmission lines. Instead of resonators 2 and 3, we now have transmission lines of a length that is an integer number of half-wavelengths ($n\lambda_g/2$). Furthermore, in the lumped element circuit, resonators 1 and 4 are connected through an inverter, we therefore need to decide what kind of connection we are going to

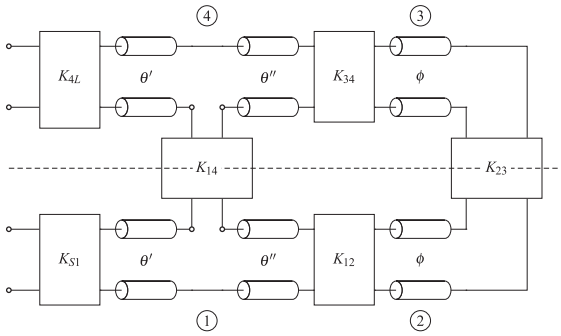

FIGURE 10. Distributed model of the 4-2 filter.

use, namely, series or parallel. Since we want to use in the real prototype an E-plane T-junction, we must use a series connection (see [20]). Therefore, the resulting equivalent distributed network is the one shown in Fig. 10 where $\phi = n \times 180°$ and $\theta' + \theta'' = n \times 180°$.

The expressions for the inverters are:

$$\begin{aligned} K_{S1} &= K_{4L} = M_{S1}\sqrt{\frac{n\pi}{2}\mathcal{W}} = M_{4L}\sqrt{\frac{n\pi}{2}\mathcal{W}} \\ K_{12} &= K_{34} = M_{12}\frac{n\pi}{2}\mathcal{W} = M_{34}\frac{n\pi}{2}\mathcal{W} \\ K_{23} &= M_{23}\frac{n\pi}{2}\mathcal{W} \\ K_{14} &= M_{14}\frac{n\pi}{2}\mathcal{W} \end{aligned} \tag{2}$$

where $\mathcal{W}$ is the fractional bandwidth (in terms of frequency if we use TEM lines or in terms of wavelength if we use waveguides).

We still have to determine the individual values for θ' and θ''. The derivation for the values of the network elements, following the procedure described in [21], results in two possible equivalent solutions $\theta' = 0°$ and $\theta' = n \times 180°$. For the time being, we will use the solution $\theta' = 0°$. The in-band response that we obtain with this choice is shown in Fig. 11 with $n = 1$, a center frequency $f_0 = 20$ GHz, and bandwidth $BW = 200$ MHz.

As we expect, there is a pair of TZs close to the pass band of the filter due to the negative 1-4 coupling. The agreement of the distributed model with the lumped model response is extremely good, even though we have used the dispersion of the TE_{10} mode of the WR-42 waveguide ($a = 10.668$ mm, $b = 4.318$ mm) in the distributed resonators.

It is interesting now look at the out-of-band response shown in Fig. 12. As we can see, there are two pairs of TZs far away below and above the pass band. This behavior is, in fact, identical to the one discussed in Section III.

It is important to note that in these simulations, we have used $n = 1$ simply to obtain a single filter response so that the additional TZs could be seen more clearly. Using $n = 3$ would have still produced the additional TZs, but would have also produced additional pass bands, just as in Figs. 7 and 8, and the additional TZs would have not been so clearly visible.

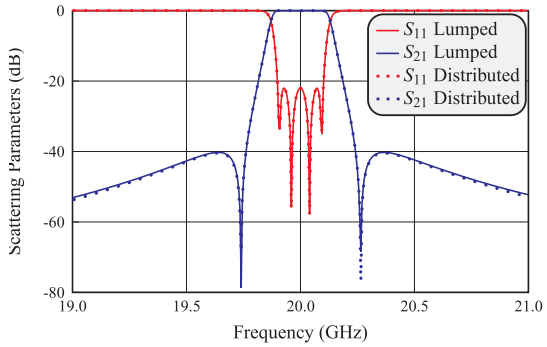

FIGURE 11. In-band response of the distributed model compared with the lumped model response given by the coupling matrix.

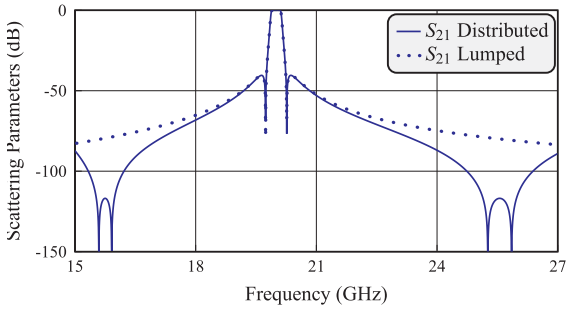

FIGURE 12. Out-of-band transmission response of the distributed model compared with the monotonically decaying response of the lumped model.

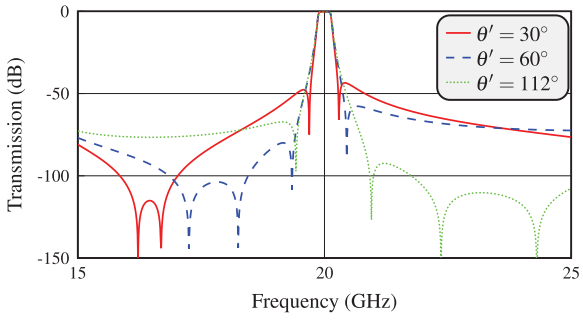

FIGURE 13. Filter performance for several values of the parameter θ'.

As already discussed in Section III, we can indeed change the frequency location of the extra zeros by simply increasing θ'. That will, of course, degrade the in-band performance, but this degradation can be compensated with a small optimization of the inverter values in order to recover the desired in-band return loss level.

An example of the influence of θ' in the location of the transmission zeros can be observed in Fig. 13, where the only parameter changed is θ'. It is important to note that, to obtain the result shown in Fig. 13 we have used again the real dispersion of the TE_{10} mode in a WR-42 waveguide.

The electrical response of Fig. 13 shows a typical near-band asymmetry when the additional TZs approach the passband. We can, however, still maintain the near-band TZs and the in-band performance with a rapid optimization

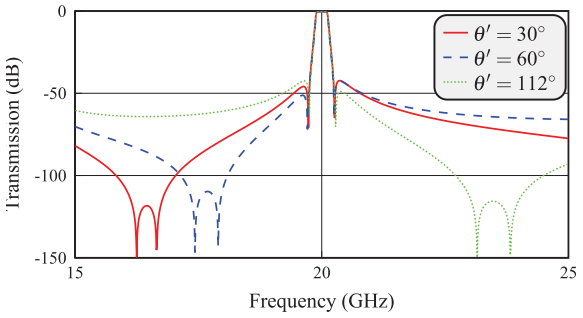

FIGURE 14. Filter performance for several values of the parameter θ' but enforcing the near-band transmission zeros at fixed frequency locations.

of the inverter values. There are, however, some limitations. If the extra TZs approach the near-band zeros, it will be difficult to maintain the TZs at the same positions and, consequently, the rejection lobe levels. It is still possible to move the parameter θ' in Fig. 13 while keeping the TZs in the same positions, through optimization of the inverter values, obtaining the result shown in Fig. 14. As we can see, the near-band TZs are now kept in their original positions.

Furthermore, it is interesting to observe that if $\theta' > 90°$ the additional transmission zeros in the higher rejection band can be moved closer to the filter pass band, as it is shown in Fig. 14.

Once we decide the location of the transmission zeros, the remaining dimensions can be extracted using the distributed model as described in [21]. It is important to note that this specific feature of the basic filter structure we are discussing can be very effectively exploited in the diplexer design.

Finally, the resonators have been designed using the TE_{103} mode in order to increase the quality factor (using $n = 3$ in (2)). To summarize, the features of the structure that we propose are:

- The number of TZs implemented is $N_{TZ} = 4$. Two are given by the coupling matrix, and are placed one below and one above the pass band. The other two can be located either to the left ($\theta' < 90°$) or to the right ($\theta' > 90°$) of the pass band.
- The extra TZs can be moved together by changing θ'. However, the convergence of the optimization process becomes slower as the extra TZs are closer to the passband.
- The extra TZs can only be moved together and cannot be allocated separately. This is because we have at our disposal only two geometrical parameters, namely the length θ', and the strength of the capacitive coupling.

V. LOW-ACCURACY DIPLEXER DESIGN

To continue with the diplexer design, we now use the structure just described to design the two separate ideal waveguide filters that fit the specifications of the two channels of the diplexers. The design has been carried out using FEST3D

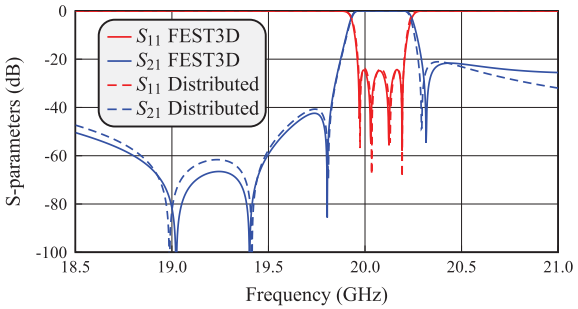

FIGURE 15. Response of the quadruplet filter for the diplexer with three TZs in the lower band. Solid lines correspond to the EM response and dashed lines correspond to the distributed model response.

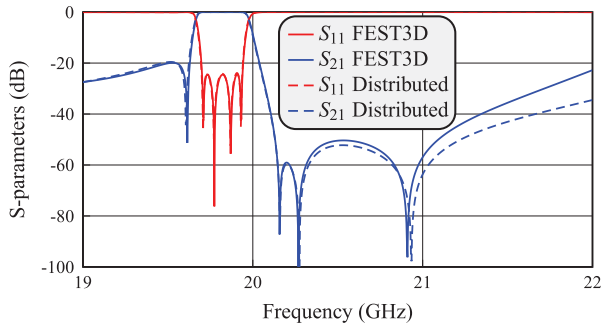

FIGURE 16. Response of the quadruplet filter for the diplexer with three TZs in the upper band. Solid lines correspond to the EM response and dashed lines correspond to the distributed model response.

(from AuroraSat, now with CST and Dassault Systèmes). The procedure is as follows:

1) Start with the coupling matrix giving the in-band performance and the near-band TZs.
2) Use the distributed model to increase θ' until the extra TZs are located where desired.
3) Optimize the inverter values to retrieve the in-band response and the near-band TZs where desired. This stage is very fast since we work only with the distributed model. No EM optimization is required at this point.
4) The initial physical dimensions of the structure are then obtained following the standard procedure described in [21]. At this point the EM simulations are performed over individual parts of the filter. Therefore, this step is also very fast.
5) We can now assemble the whole filter and perform a full-wave simulation. This will give a very good initial point for the EM optimization. With a few iterations, the optimization will now produce a response that is very close to the one given by the ideal distributed model.

At the end of the design process, we obtain two separate filters. Fig. 15 and Fig. 16 show the performance of the two separate filters compared with the distributed model. To continue with the design process, we now need to join the two filters in order to obtain a diplexer. After exploring a

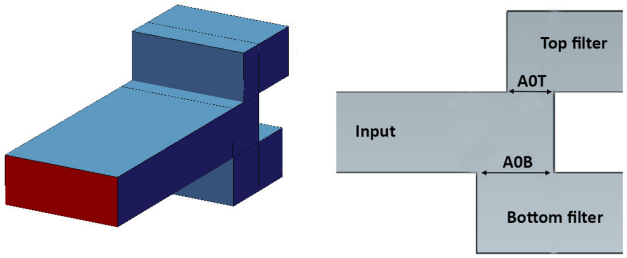

FIGURE 17. E-field T-junction implemented. A0T and A0B are the design dimensions.

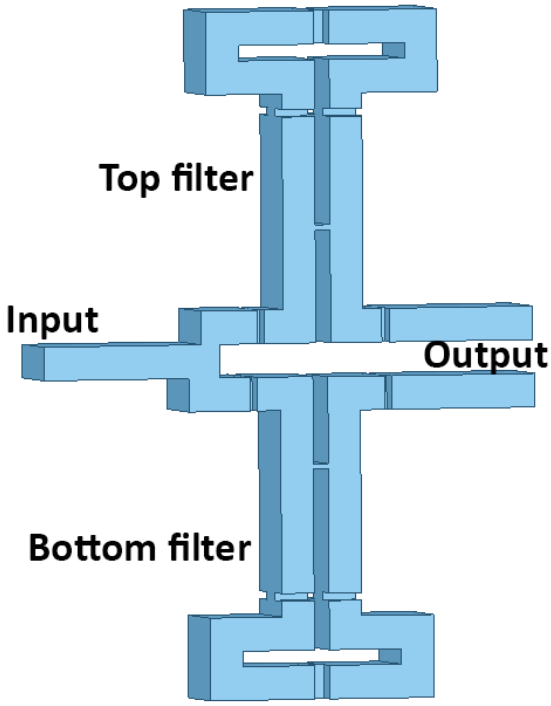

FIGURE 18. Structure of the diplexer with the T-junction.

number of possible solutions, we decided to use an E-field T-junction, as shown in Fig. 17. Fig. 18 shows the complete structure. Fig. 19 shows the initial response of the diplexer. As expected, the diplexer is not tuned correctly.

The next step is to use the procedure described in [24] to obtain the performance shown in Fig. 20. The procedure essentially consists of recovering the ideal response by optimizing the structure cavity-by-cavity.

At this point, we have a diplexer structure that satisfies all the specifications. However, all simulations performed so far have been carried out with FEST3D using a set of parameters allowing fast computations with reduced accuracy. We now need to move from a low-accuracy design to a high-accuracy design that can be successfully manufactured.

Furthermore, the diplexer we just designed uses 90° corners, and the effects of material losses have not been included. For the sake of manufacturing, it is now convenient to

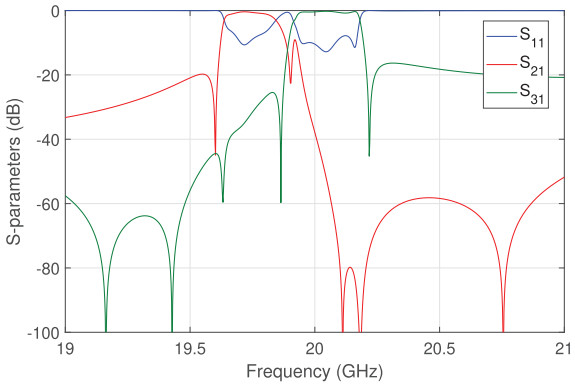

FIGURE 19. Initial response of the complete diplexer structure.

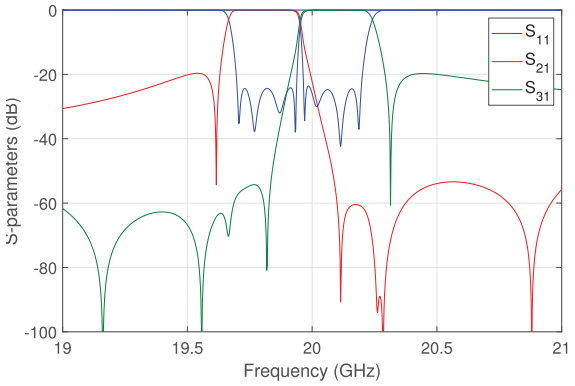

FIGURE 20. Final response of the diplexer with the T-junction.

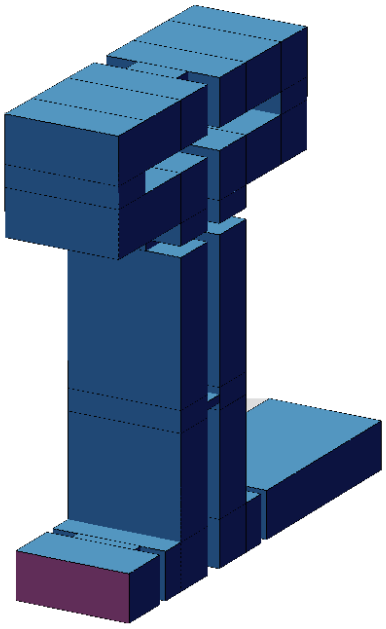

FIGURE 21. Extraction of top filter in FEST3D (coarse space).

introduce rounded corners in the structure, and to include in the simulations the losses (due to the use of aluminum in this case).

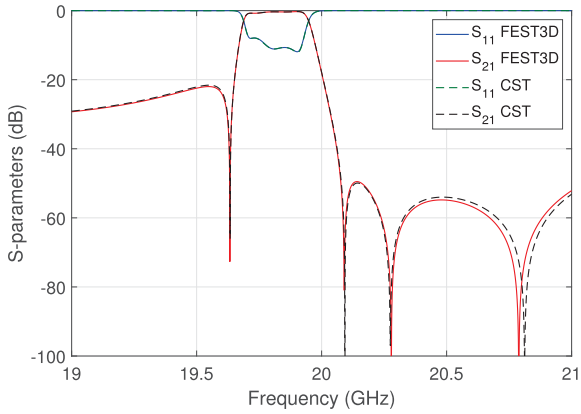

FIGURE 22. Recovered response of the top filter with sharp corners.

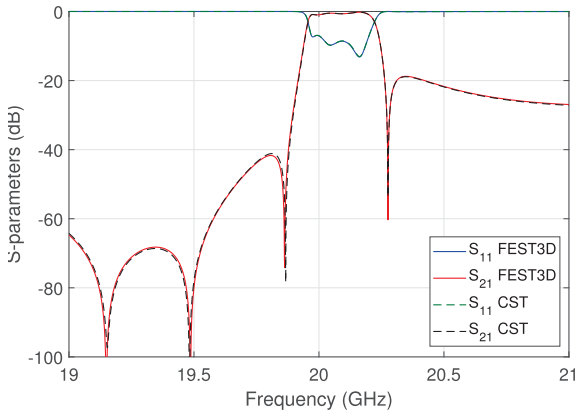

FIGURE 23. Recovered response of the bottom filter with rounded corners.

VI. HIGH-ACCURACY DIPLEXER DESIGN

The software used to carry out the high-accuracy design is CST. One possible approach could be a direct optimization using CST.

This approach, however, is extremely time-consuming due to the complexity of the hardware. A much more efficient procedure is as follows:

1) The first step consists in separating the individual filters of the diplexer shown in Fig. 18. After the separation, each filter becomes a 2-port network that can be treated independently. The 2-port structures are then simulated with the high-accuracy simulator. Naturally, the CST response will differ from the ideal one. The ASM-based procedure described in [25] is now applied to recover the ideal response,. The coarse space in this case is the one shown in Fig. 21, the fine space is the model in CST. After three iterations, the desired performance is obtained in the high-accuracy simulator. Fig. 22 shows the final response obtained with CST as compared to the ideal low-accuracy result obtained with FEST3D.
2) The following step is to add round corners to the cavities and simulate again each filter with the high-accuracy simulator. In this case, three iterations of

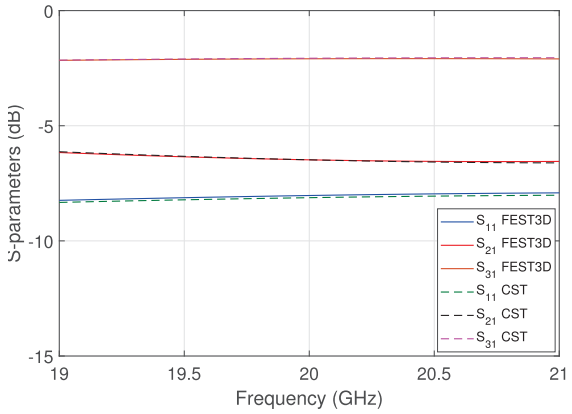

FIGURE 24. Recovered response of the T-junction.

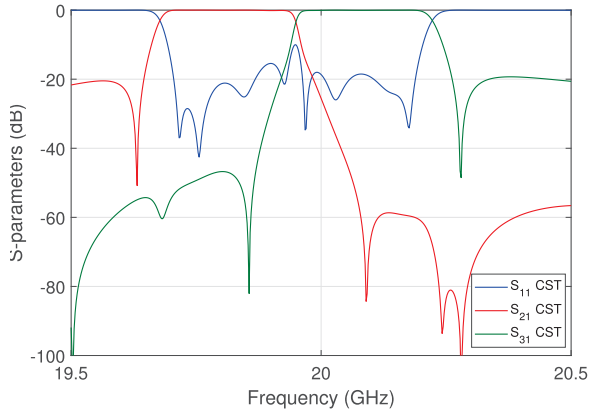

FIGURE 25. Initial response of the diplexer in CST after assembly of the separate components.

the procedure described in [25] are sufficient to recover the ideal performance. The final response of one of the filters is shown in Fig. 23.

3) Following a similar procedure, the T-junction shown in Fig. 18 is now extracted and treated as an isolated 3-port network (see Fig. 17). After adding the round corners, the T-junction is simulated in CST. The same procedure described before is used to recover the ideal T-junction response. Fig. 24 shows the final response in CST as compared to the ideal performance obtained with FEST3D.
4) After the two filters and the T-junction have been designed separately, the three parts are combined and simulated with CST. Fig. 25 shows the initial response after assembling the diplexer. This last high-accuracy result includes also the losses due to aluminum. Only one more ASM iteration is now enough to obtain the final response.

As a final verification of our design, we now simulate the final diplexer structure with HFSS (from Ansys).

As we can see in Fig. 26, the CST and HFSS simulations are almost exactly coincident. Therefore, we can conclude that we have obtained a diplexer structure that is ready to be manufactured.

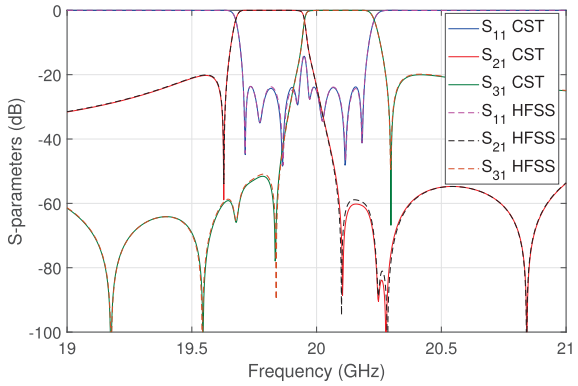

FIGURE 26. Comparison of the response of the final diplexer produced by CST and HFSS.

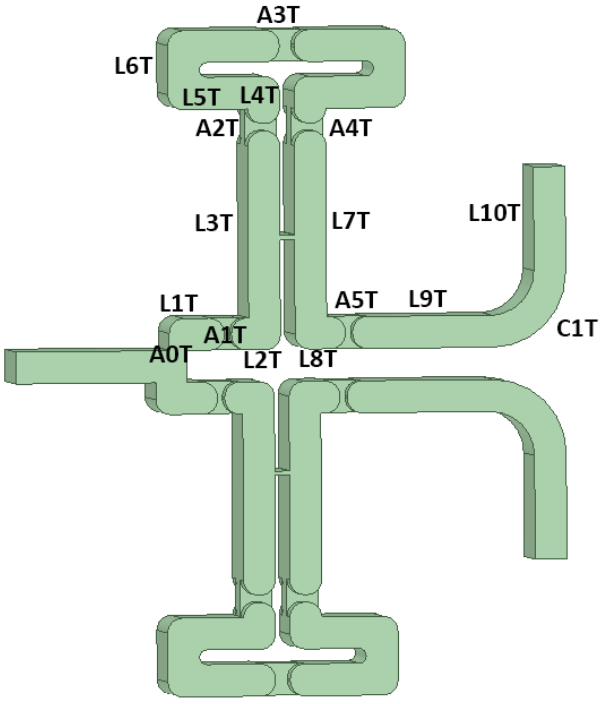

FIGURE 27. Final structure of the diplexer. Dimensions (symmetric) refer to the bottom filter, namely XXB.

Finally, one last modification has been introduced, that is to extend the output waveguide from the two filters of the diplexer in opposite directions. This has been done in order to have enough space for the connection of the waveguide flanges needed to measure the device. This modification, however, does not affect the performance of the diplexer. Fig. 27, Table 1 and Table 2, show the final structure and the dimensions of the diplexer, respectively.

To conclude this section, we show in Fig. 28 broadband performance of the device computed with CST. As we can see, the diplexer does have a very good out-of-band rejection between 18 and 22 GHz.

VII. MULTIPACTOR BREAKDOWN PREDICTION

The multipactor effect is one of the main problems that affects high power satellite devices [26]. A multipactor analysis it

TABLE 1. Dimensions of the top filter of the diplexer in millimeters.

Structure[1]	Height	Width	Length
Aperture A0T	0	10.668	2.448
Input L1T	4.318	10.668	7.471
Inductive aperture A1T	4.318	6.442	1
Cavity 1 L2T	4.318	10.668	6.648
Cavity 1 L3T	29.537	10.668	4.318
Capacity aperture[2]	0.7	10.668	2
Inductive aperture A2T	1	4.509	4.318
Cavity 2 L4T	6.318	10.668	4.318
Cavity 2 L5T	4.318	10.668	15.193
Cavity 2 L6T	10.636	10.668	4.318
Inductive aperture A3T	4.318	5.074	2
Inductive aperture A4T	1	4.727	4.318
Cavity 4 L7T	29.502	10.668	4.318
Cavity 4 L8T	4.318	10.668	6.833
Inductive aperture A5T	4.318	6.332	1
Output L9T	4.318	6.332	17.05
Output L10T[3]	4.318	6.332	14

[1] The diplexer has XY-plane symmetric dimension in L4T, L5T and L6T. All the corners are 2 mm rounded.
[2] The capacitive aperture is placed in the filter at 16.959 mm from the center axis of the diplexer.
[3] The curve C1T is a 10 mm length of rectangular waveguide with 10 mm of radius.

TABLE 2. Dimensions of the bottom filter of the diplexer in millimeters.

Structure[1]	Height	Width	Length
Aperture A0B	0	10.668	4.321
Input L1B	4.318	10.668	8.377
Inductive aperture A1B	4.318	5.871	1
Cavity 1 L2B	4.318	10.668	6.755
Cavity 1 L3B	28.801	10.668	4.318
Capacity aperture[2]	0.5	10.668	2
Inductive aperture A2B	1	4.643	4.318
Cavity 2 L4B	6.318	10.668	4.318
Cavity 2 L5B	4.318	10.668	14.666
Cavity 2 L6B	10.636	10.668	4.318
Inductive aperture A3B	4.318	4.979	2
Inductive aperture A4B	1	4.629	4.318
Cavity 4 L7B	28.807	10.668	4.318
Cavity 4 L8B	4.318	10.668	6.927
Inductive aperture A5B	4.318	6.006	1
Output L9B	4.318	6.332	17.05
Output L10B[3]	4.318	6.332	14

[1] The diplexer has XY-plane symmetric dimension in L4B, L5B and L6B. All the corners are 2 mm rounded.
[2] The capacitive aperture is placed in the filter at 14.321 mm from the center axis of the diplexer.
[3] The curve C1B is a 10 mm length of rectangular waveguide with 10 mm of radius.

therefore mandatory [27]. To carry out this analysis we will use SPARK3D (from AuroraSat, now with Dassault Systèmes). For the sake of efficiency, the usual procedure is to focus the simulations in the areas where the multipactor effect can be expected. In order to identify these areas we need to know two key data, namely, the frequencies where the group

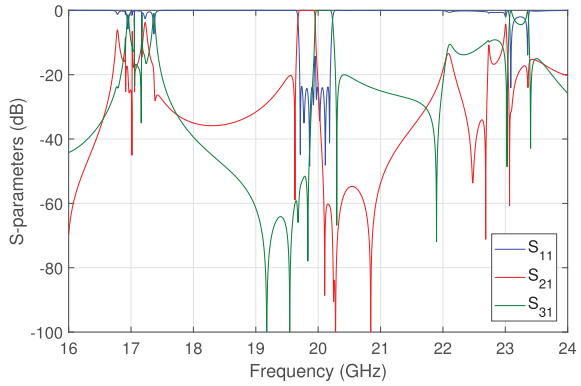

FIGURE 28. CST broadband performance of the diplexer.

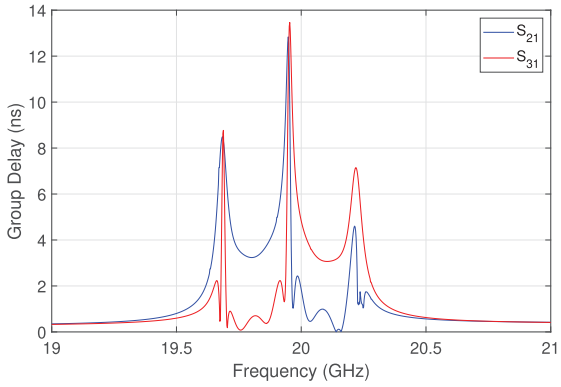

FIGURE 29. Group delay response of the diplexer.

delay is maximum for both filters, and where the E-field maximum is located at those frequencies. This information will give us and idea of where the multipactor effect may be expected.

The critical frequencies for the diplexer are 19.69 GHz, 19.95 GHz and 20.24 GHz, as shown in Fig. 29.

We now simulate the behavior of the diplexer at each frequency, and identify the locations of the E-field maxima. Fig. 30 shows one of the simulations performed with CST. As we can see, the critical areas are the corners of the filters and the capacitive windows between cavities 1 and 4.

Now that we have all the information we need, we can perform several simulations with SPARK3D to obtain the multipactor power thresholds that can initiate multipactor effects in the device. Several different simulations have been performed to obtain the thresholds for the different areas identified. The parameters used are as follows:

- Initial number of electrons: 10000
- Multipactor criterion growth factor: 10^2
- Initial power: 100 W, 5000 W and 10000 W
- Maximum power: 5000 W, 20000 W and 30000 W

The initial number of electrons and the multipactor criterion increase factor are typical values for multipactor analysis based on multiple past simulations.

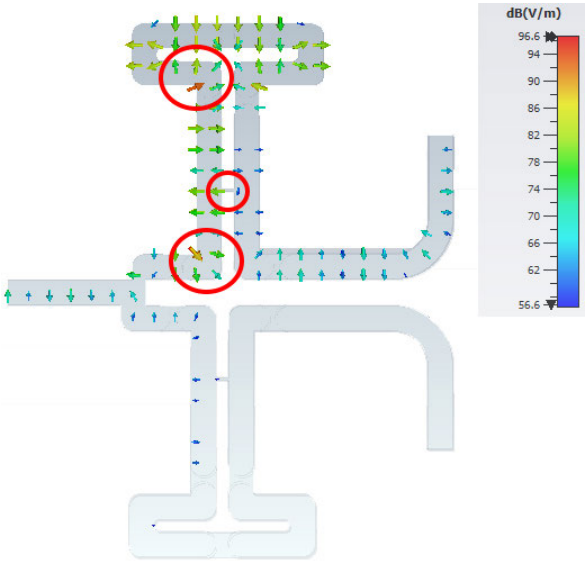

FIGURE 30. Representation of the E-field and the critical zones in the diplexer for 19.69 GHz.

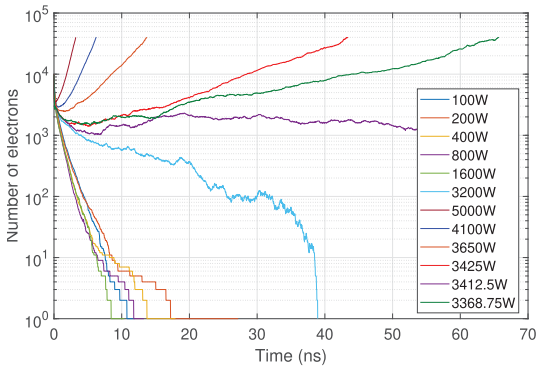

FIGURE 31. Multipactor simulation with discharges for the bottom capacitive window at 19.95 GHz.

The initial and maximum power of the analysis is usually defined by the requirements for the specific device under test. In particular, the diplexer we have designed is intended to be used as multiplexer in the satellite, with a maximum of 200 W of RF power in each channel. After each simulation, we have recorded the values for which the multipactor effect can be produced. Fig. 31 shows the result of one simulation for the capacitive window. The different lines in the graphic represents the evolution of the number of electrons in time for each different RF power level. When we have no discharges, the number of electron decreases. When the multipactor effect appears, the electron density increases in time. If the growth factor becomes greater than the multipactor growth criterion, we consider that a multipactor discharge has taken place.

Finally, Table 3 shows the power thresholds obtained with the different simulations, and the areas of the diplexer that are affected. As expected, the multipactor effect has a lower power threshold at low frequency. In addition, the multipactor effect is first generated in the capacitive window of the

TABLE 3. Power threshold of multipactor effect (in Watts).

Structure	19.69 GHz	19.95 GHz	24.24 GHz
Capacitive aperture Top	>30000	5810	7640
Capacitive aperture Bottom	>30000	3300	5820
First corner Top	>30000	>30000	>30000
Second corner Top	27185	>30000	>30000
First corner Bottom	>30000	>30000	>30000
Second corner Bottom	>30000	28750	>30000

bottom filter where the waveguide height is smaller (0.5 mm). Furthermore, the simulations indicates that we do not have any multipactor effects in the corners of the cavity filters as far as the power is below $\approx$ 30000 W. From the data we have collected, we can see that the lowest power threshold we have identified is 3300 W. This power level is definitely far above any current requirement. The diplexer can therefore be safely considered to be multipactor-free. Additionally, the diplexer has low insertion losses and has been designed following the low PIM design guidelines discussed in [28].

To conclude this section, and in order to validate the results obtained, we have performed another multipactor discharge simulation with a different simulation tool, namely, CST Particle Studio (from Dassault Systèmes). This code uses time-domain simulations to predict the multipactor thresholds. The results obtained are virtually coincident with the previous simulations and verify the results, showing a multipactor discharge in the bottom capacitive aperture around 3500 W, and at about 6600 W for the top capacitive aperture at 19.95 GHz.

VIII. MEASUREMENTS AND DISCUSSION

Finally, in order to fully validate the diplexer structure, we have manufactured a prototype. The diplexer has been fabricated in aluminum with E-plane cut in order to reduce the insertion losses. The maximum error guaranteed by the manufacturer was less than 20 microns. Fig. 32 shows the inside of the two parts of the diplexer. The final dimensions of the diplexer are $104 \times 85 \times 24$ mm with a total mass of 432 g, thus satisfying all specifications on physical dimensions and mass. It is important to mention that, we have not made any effort to produce low-weight hardware, as it is customarily done for flight hardware. The use of light-weight manufacture could, in fact, further reduce very significantly the final weight of the diplexer.

In Fig. 33 and Fig. 34 we show the breadboard of the diplexer, and the comparison between the measurements and the ideal response of the diplexer, respectively.

As we can see, the responses are practically coincident. We can, however, observe that there is a small frequency shift in the response towards lower frequencies. To further understand this aspect, we have recovered by simulation the response that we have measured with the real hardware.

The results of this analysis indicates that there is a maximum error of 17 microns. This is indeed inside the declared tolerance of 20 microns.

TABLE 4. Compared features of the referenced diplexers.

Reference	Band	Tuning screws	TZs per filter (cross-coupling)	Insertion loss	Guard band (in % of channel BW)	Fabrication
[8]	Ka	No	None	1 dB	189%	Clam-shell
[10]	Ka	No	None	2 dB	81%	Clam-shell
[11]	Ka	No	2 TZs (doublet)	Not provided	40%	Not fabricated
[12]	X	No	1 TZ (doublet)	0.35 dB	88%	Body and lid
[13]	Ku	Yes	1 TZ (triplet)	0.48 dB	190%	Body and lid
[14]	Ku	No	None	0.2 dB	323% [1]	Clam-shell
[15]	X	No	2 TZs (triplet)	Not provided	27%	Clam-shell
This work	K	No	4 TZs (quadruplet)	0.38 dB	7%	Clam-shell

[1] Guard band calculated using the BW of the RX-band channel filter.

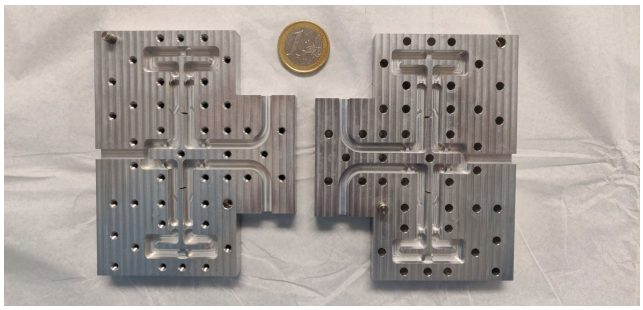

FIGURE 32. Fabricated prototype of the diplexer.

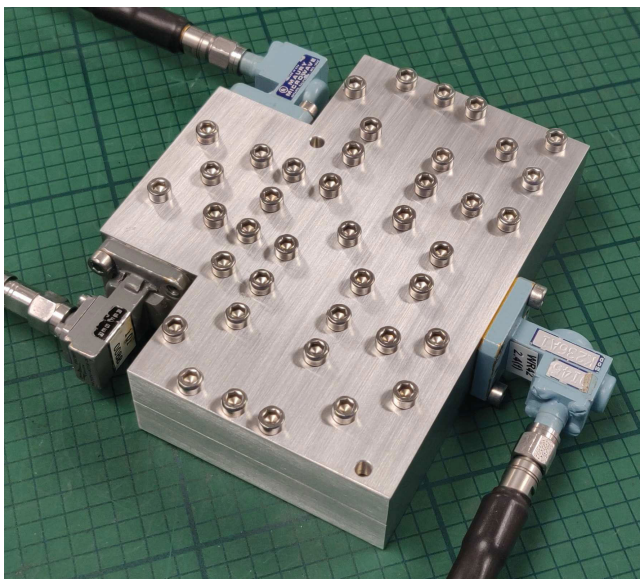

FIGURE 33. Diplexer breadboard.

Moreover, as we can observe, the S_{11} is always below 20 dB in the whole in-band response of the diplexer, as required by the specifications. The measured insertion losses, on the other hand, are 0.389 dB and 0.374 dB for the lower and higher filter, respectively. These results are close to the required specifications but are not compliant. A compliant insertion loss can, however, be easily obtained silver-plating the device.

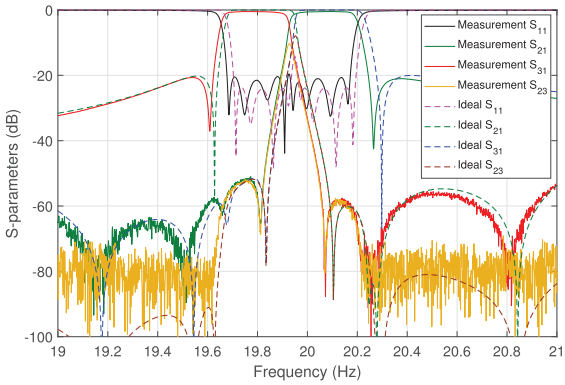

FIGURE 34. Comparison between measurement and ideal response.

Finally, the isolation requirements have been achieved for both, the contiguous edge ($\geq$ 26 dB @ CF $\pm$ 144 MHz and $\geq$ 52 dB @ CF $\pm$ 381 MHz) and the non-contiguous edge ($\geq$ 20 dB @ CF $\pm$ 192 MHz).

Table 4 provides a comprehensive comparison between the proposed diplexer and the recently reported prototypes given in the references.

The comparison clearly shows that our structure has the smallest guard band between channels, provides more TZs with low order, has low insertion losses (even without silver plating), and its high-power behavior (in terms of multipactor effect) has been successfully proven with two well-known commercial software tools.

All these characteristics make this diplexer an ideal candidate for satellite applications.

IX. CONCLUSION

In this paper, we have discussed the detailed design procedure for a diplexer structure based on the use of an E-plane T-junction together with two rectangular waveguide filters implementing quadruplets. The structure allows for the implementation of a number of TZs in the performance of the filters thus resulting in a highly selective response. The final structure is simple and very easy to manufacture. In addition, a multipactor study of the device has been carried out, indicating no multipactor problems up to 3300 W.

Finally, the performance of the diplexer has been verified successfully with several commercial simulation tools of well known accuracy, and by measurements of a prototype manufactured in aluminum. The results obtained are compliant with all of the initial specifications, except for the insertion losses (0.389/0.374 dB). However, this can be easily compensated by silver-plating the device. In conclusion, we have successfully proven that the diplexer structure we developed can be built to be fully compliant with the requirements of modern multi-beam satellite payloads.

REFERENCES

[1] S. K. Rao, "Advanced antenna technologies for satellite communications payloads," *IEEE Trans. Antennas Propag.*, vol. 63, no. 4, pp. 1205–1217, Apr. 2015.

[2] H. Fenech, S. Amos, A. Tomatis, and V. Soumpholphakdy, "High throughput satellite systems: An analytical approach," *IEEE Trans. Aerosp. Electron. Syst.*, vol. 51, no. 1, pp. 192–202, Jan. 2015.

[3] G. Maral and M. Bousquet, *Satellite Communication Systems*, 5th ed. Chichester, U.K.: Wiley, 2009.

[4] C. Kudsia, R. Cameron, and W.-C. Tang, "Innovations in microwave filters and multiplexing networks for communications satellite systems," *IEEE Trans. Microw. Theory Techn.*, vol. 40, no. 6, pp. 1133–1149, Jun. 1992.

[5] R. J. Cameron, C. M. Kudsia, and R. R. Mansour, *Microwave Filters for Communication Systems: Fundamentals, Design and Applications*, 2nd ed. Hoboken, NJ, USA: Wiley, 2018.

[6] J. Uher, J. Bornemann, and U. Rosenberg, *Waveguide Components for Antenna Feed Systems: Theory and CAD*. Norwood, MA, USA: Artech House, 1993.

[7] A. Morini and T. Rozzi, "Analysis of compact E-plane diplexers in rectangular waveguide," *IEEE Trans. Microw. Theory Techn.*, vol. 43, no. 8, pp. 1834–1839, Aug. 1995.

[8] Y. Rong, H.-W. Yao, K. A. Zaki, and T. G. Dolan, "Millimeter-wave ka-band H-plane diplexers and multiplexers," *IEEE Trans. Microw. Theory Techn.*, vol. 47, no. 12, pp. 2325–2330, Dec. 1999.

[9] J. M. Rebollar, J. R. Montejo-Garai, and A. Onoro, "Asymmetric H-plane T-junction for broadband diplexer applications," in *IEEE AP-S Int. Symp. Dig.*, Jul. 2000, pp. 2032–2035.

[10] T. Shen, K. A. Zaki, and T. G. Dolan, "Rectangular waveguide diplexers with a circular waveguide common port," *IEEE Trans. Microw. Theory Techn.*, vol. 51, no. 2, pp. 578–582, Feb. 2003.

[11] E. Ofli, R. Vahldieck, and S. Amari, "Novel E-plane filters and diplexers with elliptic response for millimeter-wave applications," *IEEE Trans. Microw. Theory Techn.*, vol. 53, no. 3, pp. 843–851, Mar. 2005.

[12] S. Bastioli, L. Marcaccioli, and R. Sorrentino, "An original resonant Y-junction for compact waveguide diplexers," in *IEEE MTT-S Int. Microw. Symp. Dig.*, Jun. 2009, pp. 1233–1236.

[13] L. Zhu, R. R. Mansour, and M. Yu, "A compact waveguide diplexer employing dual-band resonators," in *IEEE MTT-S Int. Microw. Symp. Dig.*, Jun. 2014, pp. 1–4.

[14] F. Teberio, I. Arregui, M. Guglielmi, A. Gomez-Torrent, P. Soto, M. A. G. Laso, and V. E. Boria, "Compact broadband waveguide diplexer for satellite applications," in *IEEE MTT-S Int. Microw. Symp. Dig.*, May 2016, pp. 1–4.

[15] U. Rosenberg, M. Knipp, and S. Amari, "Compact diplexer design using different E-Plane triplets to serve contiguous passbands with high interband selectivity," in *Proc. Eur. Microw. Conf.*, Sep. 2006, pp. 133–136.

[16] L. Accatino, G. Bertin, and G. Macchiarella, "A compact waveguide filtering structure with transmission zeros for multi-beam satellites," in *IEEE MTT-S Int. Microw. Symp. Dig.*, Jun. 2017, pp. 737–740.

[17] J. Ossorio, S. Cogollos, V. Boria, and M. Guglielmi, "Rectangular waveguide quadruplet filter for satellite applications," in *IEEE MTT-S Int. Microw. Symp. Dig.*, Jun. 2019, pp. 1359–1362.

[18] *Lightweight and Compact Diplexer for Multibeam Payloads*, document ESA-ESTEC Document AO/1-7447/13/NL/EM (ITT), ARTES 5.1, 2013.

[19] C. Carceller, P. Soto, V. Boria, and M. Guglielmi, "Capacitive obstacle realizing multiple transmission zeros for in-line rectangular waveguide filters," *IEEE Microw. Wireless Compon. Lett.*, vol. 26, no. 10, pp. 795–797, Oct. 2016.

[20] N. Marcuvitz, "Waveguide handbook," in *IEE Electromagnetic Waves*, vol. 21. Stevenage, U.K.: Peter Peregrinus Ltd., 1986.

[21] S. Cogollos, M. Brumos, V. E. Boria, C. Vicente, J. Gil, B. Gimeno, and M. Guglielmi, "A systematic design procedure of classical dual-mode circular waveguide filters using an equivalent distributed model," *IEEE Trans. Microw. Theory Techn.*, vol. 60, no. 4, pp. 1006–1017, Apr. 2012.

[22] M. Guglielmi and A. A. Melcon, "Novel design procedure for microwave filters," in *Proc. 23rd Eur. Microw. Conf.*, Oct. 1993, pp. 212–213.

[23] J. W. Bandler, R. M. Biernacki, S. Hua Chen, R. H. Hemmers, and K. Madsen, "Electromagnetic optimization exploiting aggressive space mapping," *IEEE Trans. Microw. Theory Techn.*, vol. 43, no. 12, pp. 2874–2882, Dec. 1995.

[24] M. Guglielmi, "Simple CAD procedure for microwave filters and multiplexers," *IEEE Trans. Microw. Theory Techn.*, vol. 42, no. 7, pp. 1347–1352, Jul. 1994.

[25] J. Ossorio, J. C. Melgarejo, V. E. Boria, M. Guglielmi, and J. W. Bandler, "On the alignment of low-fidelity and High- fidelity simulation spaces for the design of microwave waveguide filters," *IEEE Trans. Microw. Theory Techn.*, vol. 66, no. 12, pp. 5183–5196, Dec. 2018.

[26] A. Woode and J. Petit, *Diagnostic Investigations into the Multipactor Effect, Susceptibility Zone Measurements and Parameters Affecting a Discharge*. Noordwijk, The Netherlands: ESA, Nov. 1989.

[27] *Multipacting Design Test*, document ECSS-20-01A, European Cooperation for Space Standarization (ECSS), ESA-ESTEC, ESA Publication Division, The Netherlands, May 2003.

[28] D. Smacchia, P. Soto, V. E. Boria, M. Guglielmi, C. Carceller, J. R. Garnica, J. Galdeano, and D. Raboso, "Advanced compact setups for passive intermodulation measurements of satellite hardware," *IEEE Trans. Microw. Theory Techn.*, vol. 66, no. 2, pp. 700–710, Feb. 2018.

JAVIER OSSORIO GARCÍA was born in Valencia, Spain, in March 1992. He received the degree and double master's degrees in telecommunications engineering from the Universitat Politècnica de València, Spain, in 2014 and 2016, respectively, where he is currently pursuing the Ph.D. degree in telecommunications with the iTEAM group. His current research interests include EM simulations of waveguide filters, efficient design and optimizations of waveguide filters, and development of new tunable structure filters for satellite applications.

JUAN CARLOS MELGAREJO LERMAS was born in Alicante, Spain, in 1993. He received the bachelor's degree in telecommunications from the Universitat Politècnica de València, in 2015 and the double master's degree in telecommunications systems from UPV. In 2017, he began his Ph.D. degree at the university, where his main research interests have been investigating microwave passive devices and manufacturing techniques for satellite components.

SANTIAGO COGOLLOS (Member, IEEE) was born in Valencia, Spain, in January 1972. He received the degree in telecommunication engineering and the Ph.D. degree from the Universitat Politècnica de València (UPV), Valencia, in 1996 and 2002, respectively. In 2000, he joined the Communications Department, Universitat Politècnica de València, where he was an Assistant Lecturer, from 2000 to 2001, a Lecturer, from 2001 to 2002, and became an Associate Professor, in 2002. He has collaborated with the European Space Research and Technology Centre of the European Space Agency in the development of modal analysis tools for payload systems in satellites. In 2005, he held a postdoctoral research position working in the area of new synthesis techniques in filter design at the University of Waterloo, Waterloo, ON, Canada. His current research interests include applied electromagnetics, mathematical methods for electromagnetic theory, analytical and numerical methods for the analysis of microwave structures, and design of waveguide components for space applications.

VICENTE E. BORIA (Fellow, IEEE) was born in Valencia, Spain, in May 1970. He received the Ingeniero de Telecomunicación degree (Hons.) and the Doctor Ingeniero de Telecomunicación degree from the Universitat Politècnica de València, Valencia, in 1993 and 1997, respectively. In 1993 he joined the Departamento de Comunicaciones, Universitat Politècnica de València, where he has been a Full Professor, since 2003. In 1995 and 1996, he was holding a Spanish Trainee position with the European Space Research and Technology Centre, European Space Agency (ESTEC-ESA), Noordwijk, The Netherlands, where he was involved in the area of EM analysis and design of passive waveguide devices. He has authored or coauthored ten chapters in technical textbooks, 180 articles in refereed international technical journals, and over 200 articles in international conference proceedings. His current research interests are focused on the analysis and automated design of passive components, left-handed and periodic structures, as well as on the simulation and measurement of power effects in passive waveguide systems. He acts as a Regular Reviewer of the most relevant IEEE and IET technical journals on his areas of interest. Dr. Boria has also been a member of the IEEE Microwave Theory and Techniques Society (IEEE MTT-S) and the IEEE Antennas and Propagation Society (IEEE AP-S), since 1992. He is also member of the European Microwave Association (EuMA). He is also a member of the Technical Committees of the IEEE-MTT International Microwave Symposium and of the European Microwave Conference. He has been the Chair of the 48th European Microwave Conference held in Madrid, Spain. He had been an Associate Editor of the IEEE Microwave and Wireless Components Letters, from 2013 to 2018, and *IET Electronics Letters*, from 2015 to 2018. He also serves as a Subject Editor (Microwaves) for *IET Electronics Letters*, and as an Editorial Board member for the *International Journal of RF and Microwave Computer-Aided Engineering*.

MARCO GUGLIELMI (Life Fellow, IEEE) was born in Rome, Italy, in December 1954. He received the Laurea degree in ingegneria elettronica from the University of Rome La Sapienza, Rome, in 1979, where he attended the Scuola di Specializzazione in Elettromagnetismo Applicato, in 1980, the M.S. degree in electrical engineering from the University of Bridgeport, Bridgeport, CT, USA, in 1982, and the Ph.D. degree in electrophysics from Polytechnic University, Brooklyn, NY, USA, in 1986. From 1984 to 1986, he was an Academic Associate with Polytechnic University, where he was an Assistant Professor, from 1986 to 1988. From 1988 to 1989, he was an Assistant Professor with the New Jersey Institute of Technology, Newark, NJ, USA. In 1989, he joined the European Space Agency as a Senior Microwave Engineer at the RF System Division, European Space Research and Technology Centre (ESTEC), Noordwijk, The Netherlands, where he was in charge of the development of microwave filters and electromagnetic simulation tools. In 2001, he was appointed the Head of the Technology Strategy Section, ESTEC, where he contributed to the development of management processes and tools for the formulation of a European strategy for Space Technology Research and Development. In 2014, he retired from the European Space Agency. He is also holding the position of Invited Senior Researcher with the Polytechnic University of Valencia, Valencia, Spain. Dr. Guglielmi has been elevated to the grade of Fellow of the IEEE in January 2013 for contributions to multimode equivalent networks and microwave filter design. In 1981, he was awarded a Fulbright Scholarship, Rome, and the Halsey International Scholarship Programme (HISP) from the University of Bridgeport.